

# On the Use of the Geometric Mean in FDTD Near-to-Far-Field Transformations

Dirk J. Robinson and John B. Schneider, *Member, IEEE*

**Abstract**—Near-to-far-field transformations require the tangential electric and magnetic fields over a surface, which we call the integration boundary. However, the staggered nature of the finite-difference time-domain grid is problematic in that the electric and magnetic fields are not collocated in either space or time. For harmonic transformations, i.e., ones which rely upon a Fourier transform of the time-domain near-fields, one can account for the temporal offset with a simple phase correction in the frequency domain. To account for spatial offsets, previously an arithmetic mean of the time-domain fields to either side of the integration boundary has been used. Here we show that superior results are obtained by instead using a geometric mean of the harmonic fields to either side of the integration boundary.

**Index Terms**—Finite-difference time-domain (FDTD) methods.

## I. INTRODUCTION

THE surface equivalence theorem allows one to convert an inhomogeneous region containing arbitrary scatterers and sources into a homogeneous region such that the fields exterior to the region are unaltered [1], [2]. To accomplish this, a fictitious surface, which we label the integration boundary, is defined which bounds all the inhomogeneities and scatterers. The fields interior to the integration boundary are then set to zero. The discontinuity between the fields interior and exterior to the boundary is accounted for via the use of electric and magnetic surface currents. Because the fields are zero in the interior, the region can now be assumed to be homogeneous.

In the continuous world, given the surface currents over the integration boundary and given that the surrounding medium is homogeneous, calculating the far-fields radiated by the currents is straightforward (see, e.g., [2]). The finite-difference time-domain (FDTD) method readily provides the near-fields associated with a given scattering or radiation problem. However, in the discrete world of the FDTD method the transformation of those fields to the far-field is not necessarily straightforward. Nevertheless, various authors have successfully implemented such a transform [3]–[6]. Initially harmonic excitation was used to determine the surface currents over the integration boundary but Furse *et al.* [7] showed how results could be obtained efficiently at several frequencies by using pulsed illumination and a “running” discrete Fourier transform (DFT) to obtain the equivalent surface currents.

With proper consideration, the medium exterior to the integration boundary need not be homogeneous. Demarest *et al.*

[8] and Huang *et al.* [9] described an FDTD frequency-domain near-to-far-field (NTFF) transformation for scatterers buried in stratified media. Sullivan and Young [10] discussed a method for calculating the fields radiated from an aperture. This approach merely required the fields over the aperture itself, i.e., it exploited image theory so that only a single field was needed. Kunz [11] also discussed the use of a transformation based on a single field.

In this paper, we are interested in using the time-domain near-fields to determine the harmonic far-fields at a few discrete frequencies. This approach allows one to easily calculate the scattering in any direction. However, alternate transformations exist which permit the direct calculation of the time-domain far-fields (but these transforms do not readily yield the scattering in multiple directions). Such a technique was first presented by Britt [12]. Independent work by others provided more detail and expanded on the subject [10], [13]–[17]. A 2-D time-domain transformation, which is arguably much more difficult to implement than a 3-D one owing to the infinitely long impulse response, was presented by Kragalott *et al.* [18].

A good discussion of FDTD NTFF transformations can be found in [19]. The interested reader is directed there for further details concerning the implementation for both harmonic and time-domain transforms.

Recently a modification to the common implementation of harmonic NTFF transformations was presented by Li *et al.* [20]. This modification was used to improve the accuracy of the transform when calculating the backscattering from strongly forward-scattering objects. This modification entailed discarding the surface currents on the forward-scattering face. Because the fields are large on the forward face, they can corrupt the backscattered fields which are orders of magnitude smaller than the forward-scattered field. As will be shown, the technique proposed here provides superior results to the modification proposed by Li *et al.* and does not require discarding any data.

The technique proposed here, which we label the geometric-mean near-to-far-field (GM-NTFF) transform, provides a better way to account for the fact that one cannot collocate both the tangential electric and magnetic fields on the integration boundary over which the near-fields are measured. The use of the geometric mean is motivated by the previous work of Fang and Xue [21] (see further discussion in [22] and [23]). Fang and Xue showed that when calculating impedances the geometric mean of the harmonic fields provided greater accuracy than did the arithmetic mean of the time-domain fields. The use of the geometric mean can be readily applied in the context of NTFF transforms and, as will be demonstrated, can provide significant improvements over the arithmetic mean.

Manuscript received June 8, 2006; revised June 4, 2007. This work was supported in part by the Office of Naval Research Code 3210A.

The authors are with the School of Electrical Engineering and Computer Science, Washington State University, Pullman, WA 99164-2752 USA (e-mail: zarg@wsu.edu; schneidj@eecs.wsu.edu).

Digital Object Identifier 10.1109/TAP.2007.908795

The following section provides a brief discussion of the relevant aspects of FDTD NTFF transforms and the reasons why the geometric mean works well. Section III provides results for various problems which demonstrate the improved accuracy of the GM-NTFF transform. Conclusions appear in Section IV.

## II. GEOMETRIC-MEAN NEAR-TO-FAR-FIELD TRANSFORMATION

NTFF transforms typically require knowledge of both the tangential electric and magnetic fields over a surface, i.e., the integration boundary, which bounds the scatterer or radiating sources. As an example, in two dimensions, the electric field  $\hat{\mathbf{E}}$  at the far-field point  $\boldsymbol{\rho}$  can be obtained from the scattered “near” fields using [2]

$$\hat{\mathbf{E}}(\boldsymbol{\rho}) = \sqrt{\frac{j}{8\pi\beta}} \frac{e^{-j\beta\rho}}{\sqrt{\rho}} \left\{ \mathbf{a}_\phi(\omega\mu_0\hat{\mathbf{N}}_{2D} \cdot \mathbf{a}_\phi + \beta\hat{\mathbf{L}}_{2D} \cdot \mathbf{a}_z) - \mathbf{a}_z(\omega\mu_0\hat{\mathbf{N}}_{2D} \cdot \mathbf{a}_z - k\hat{\mathbf{L}}_{2D} \cdot \mathbf{a}_\phi) \right\} \quad (1)$$

where

$$\hat{\mathbf{N}}_{2D} = \oint_L \hat{\mathbf{J}}(\boldsymbol{\rho}') e^{j\beta\rho' \cos\psi} d\ell' \quad (2)$$

$$\hat{\mathbf{L}}_{2D} = \oint_L \hat{\mathbf{M}}(\boldsymbol{\rho}') e^{j\beta\rho' \cos\psi} d\ell' \quad (3)$$

$\beta$  is the wavenumber,  $L$  is the closed path of integration, and  $\psi$  is the angle between the source point and observation point. Unprimed coordinates correspond to the observation point while primed coordinates indicate the “source” location (i.e., points along the integration path). The electric and magnetic surface currents are given by

$$\hat{\mathbf{J}}(\boldsymbol{\rho}') = \mathbf{n} \times \hat{\mathbf{H}}(\boldsymbol{\rho}') \quad (4)$$

$$\hat{\mathbf{M}}(\boldsymbol{\rho}') = -\mathbf{n} \times \hat{\mathbf{E}}(\boldsymbol{\rho}') \quad (5)$$

where  $\mathbf{n}$  is a unit vector outward normal to the integration contour. A carat indicates a quantity in the frequency domain. The challenge in an FDTD simulation is reconciling the fact that the electric and magnetic fields are offset in both space and time and yet the surface currents needed in the NTFF transformation must be collocated in space and use the same phase reference.

Fig. 1 depicts an integration boundary in a  $\text{TM}^z$  grid. The boundary is assumed to be aligned with the electric-field nodes, i.e., the  $E_z$  nodes. The expanded views show a portion of the boundary along the right side and the bottom. The field notation employs superscripts to indicate time steps while spatial indexes are given as arguments within parentheses. Half-step spatial offsets are implicitly understood. Thus, the nodes in space-time and the corresponding notation are

$$H_x^{(q-1/2)\Delta_t}(m\Delta_x, [n+1/2]\Delta_y) = H_x^{q-1/2}(m, n) \quad (6)$$

$$H_y^{(q-1/2)\Delta_t}([m+1/2]\Delta_x, n\Delta_y) = H_y^{q-1/2}(m, n) \quad (7)$$

$$E_z^{q\Delta_t}(m\Delta_x, n\Delta_y) = E_z^q(m, n) \quad (8)$$

where  $\Delta_x$  and  $\Delta_y$  are the spatial steps in the  $x$  and  $y$  directions, respectively, and  $\Delta_t$  is the temporal step. The index  $q$  indicates

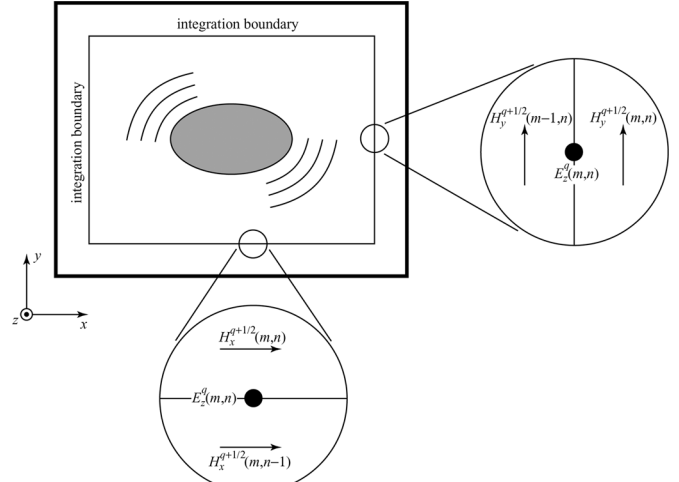


Fig. 1. Depiction of a  $\text{TM}^z$  grid showing the integration boundary. The boundary is assumed to be aligned with electric-field nodes. The expanded views show the offset of the magnetic-field nodes from the boundary.

the temporal step and we assume it varies between 1 and  $N_T$  which is the total number of time-steps.

NTFF transforms require that the fields be defined over a single surface and use the same phase reference. For harmonic fields, the temporal offset can be easily accounted for with a phase factor. Assume the magnetic fields have been recorded at times of  $q = 1/2, 3/2, 5/2, \dots$ , while the electric field has been recorded at times of  $q = 1, 2, 3, \dots$ . For the harmonic transforms of interest here, the time-domain near-fields are Fourier transformed to the frequency domain. For example, the harmonic electric field on the boundary is given by

$$\hat{E}_z^k(m, n) = \mathcal{F}[E_z^q(m, n)] \quad (9)$$

$$= \frac{1}{N_T} \sum_{q=\langle N_T \rangle} E_z^q(m, n) e^{-jk \frac{2\pi}{N_T} q} \quad (10)$$

where  $\mathcal{F}$  is the discrete Fourier transform. For situations where the entire spectrum is not of interest, typically a running discrete Fourier transform will be used only at the particular frequencies of interest. A frequency is specified by the index  $k$  which varies between zero (dc) and  $N_T - 1$ . Regardless of the implementation used, the resulting spectral terms  $\hat{E}_z^k$  will be the same.

The time-domain series  $E_z^q(m, n)$  can be obtained from  $\hat{E}_z^k(m, n)$  via

$$E_z^q(m, n) = \sum_{k=\langle N_T \rangle} \hat{E}_z^k(m, n) e^{jk \frac{2\pi}{N_T} q}. \quad (11)$$

Owing to the temporal offset between the electric and magnetic fields, one actually wants  $E_z^{q-1/2}(m, n)$ , thus, plugging  $q-1/2$  into (11) yields

$$E_z^{q-1/2}(m, n) = \sum_{k=\langle N_T \rangle} \left( \hat{E}_z^k(m, n) e^{-jk \frac{\pi}{N_T}} \right) e^{jk \frac{2\pi}{N_T} q}. \quad (12)$$

In practice one calculates  $\hat{E}_z^k(m, n)$  and the spectral representation of the magnetic fields in the same way, i.e., as in (10). Then

one multiplies  $\hat{E}_z^k(m, n)$  by  $\exp(-jk\pi/N_T)$  to account for the temporal offset.

The spatial offset is slightly more problematic than the temporal offset. As shown in Fig. 1, the integration boundary can be aligned with only one of the fields. The magnetic field tangential to the integration boundary is found from the nodes which are a half spatial step to either side of the boundary.

To obtain the magnetic field on the boundary, the traditional approach has been to use a spatial average of the nodes to either side of the boundary. For example, along the right side of the boundary, the harmonic magnetic field would be given by

$$\hat{H}_y^k(m, n) = \frac{1}{2} \mathcal{F} \left[ H_y^{q-1/2}(m-1, n) + H_y^{q-1/2}(m, n) \right]. \quad (13)$$

Because of this spatial average,  $\hat{H}_y(m, n)$  and  $\hat{E}_z(m, n)$  are assumed to be collocated and, with the temporal phase correction, can be used to determine the equivalent currents over the integration boundary (which are then used in the NTF transform itself—see [19] for details).

Unfortunately the arithmetic mean used in (13) introduces errors. To illustrate this, assume a harmonic planewave is propagating in the grid. The temporal frequency  $\omega$  is  $2\pi k'/N_T$  where  $k'$  is an integer constant and, as before,  $N_T$  is the total number of time-steps in a simulation. The  $y$  component of the magnetic field is given by

$$\begin{aligned} H_y^{q-1/2}(m, n) &= \cos \left( \omega \left[ q - \frac{1}{2} \right] \Delta_t - \xi \right) \\ &= \frac{e^{j \left( k' \frac{2\pi}{N_T} \left[ q - \frac{1}{2} \right] \Delta_t + \xi \right)} + e^{-j \left( k' \frac{2\pi}{N_T} \left[ q - \frac{1}{2} \right] \Delta_t + \xi \right)}}{2} \end{aligned} \quad (14)$$

where  $\xi = \beta_x(m+1/2)\Delta_x + \beta_y n \Delta_y$ , and  $\beta_x$  and  $\beta_y$  are the  $x$  and  $y$  components of the wave vector, respectively. Taking the discrete Fourier transform of (15), i.e.,

$$\hat{H}_y^k(m, n) = \frac{1}{N_T} \sum_{q=(N_T)} H_y^{q-1/2}(m, n) e^{-jk \frac{2\pi}{N_T} (q-\frac{1}{2})} \quad (16)$$

one notes that the sum yields zero when  $k$  is anything other than  $k'$  or  $N_T - k'$ . The values of  $k$  which yield non-zero correspond to the positive and negative frequency of the continuous world and, like the continuous world, the corresponding spectral values are complex conjugates. Without loss of generality, we will continue the discussion in terms of the spectral component corresponding to the positive frequency, i.e.,

$$\hat{H}_y^k(m, n) = \frac{1}{2} \exp(-j[\beta_x(m+1/2)\Delta_x + \beta_y n \Delta_y]). \quad (17)$$

(Note that since the time-domain functions are real-valued, in practice one does not need to calculate the transform at any of

the negative frequencies. They are merely the complex conjugates of the values at the positive frequencies.)

Because the Fourier transform is a linear operator, using (15) in (13) yields

$$\begin{aligned} \hat{H}_y^{k'}(m, n) &= e^{-j\beta_y n \Delta_y} \frac{e^{-j\beta_x(m-\frac{1}{2})\Delta_x} + e^{-j\beta_x(m+\frac{1}{2})\Delta_x}}{4} \\ &= \frac{1}{2} e^{-j(\beta_x m \Delta_x + \beta_y n \Delta_y)} \cos \left( \frac{\beta_x \Delta_x}{2} \right). \end{aligned} \quad (18)$$

The exact expression for the magnetic field on the integration boundary is  $\exp(-j[\beta_x m \Delta_x + \beta_y n \Delta_y])/2$ . Thus, the cosine term represents an error—one which vanishes only in the limit as the spatial-step size goes to zero.

Instead of taking the Fourier transform of the average of the time-domain fields, let us take the Fourier transform of the fields to either side of the boundary. We define the transforms as

$$\hat{H}_y^+(m, n) = \mathcal{F} \left[ H_y^{q-1/2}(m, n) \right] \quad (20)$$

$$\hat{H}_y^-(m, n) = \mathcal{F} \left[ H_y^{q-1/2}(m-1, n) \right]. \quad (21)$$

Still assuming a single harmonic planewave, for the “positive frequency” corresponding to  $k = k'$ ,  $\hat{H}_y^+(m, n)$  and  $\hat{H}_y^-(m, n)$  are given by

$$\hat{H}_y^+(m, n) = \frac{1}{2} e^{-j(\beta_x(m+1/2)\Delta_x + \beta_y n \Delta_y)} \quad (22)$$

$$\hat{H}_y^-(m, n) = \frac{1}{2} e^{-j(\beta_x(m-1/2)\Delta_x + \beta_y n \Delta_y)}. \quad (23)$$

Were one to calculate the arithmetic mean of  $\hat{H}_y^+(m, n)$  and  $\hat{H}_y^-(m, n)$ , the result would be the same as given in (19). However, consider the geometric mean (where the geometric mean of  $a$  and  $b$  is  $\sqrt{ab}$ ) of  $\hat{H}_y^+(m, n)$  and  $\hat{H}_y^-(m, n)$

$$\hat{H}_y^{k'}(m, n) = (\hat{H}_y^+(m, n) \hat{H}_y^-(m, n))^{1/2} \quad (24)$$

$$= \frac{1}{2} e^{-j(\beta_x m \Delta_x + \beta_y n \Delta_y)}. \quad (25)$$

This is precisely the correct answer. There is no error introduced by the geometric mean. A note of caution: when calculating the square root of these complex quantities, one must ensure that the proper branch cut is selected. Thus, when  $\hat{H}_y^+(m, n)$  and  $\hat{H}_y^-(m, n)$  have phases near  $\pm\pi$  the geometric mean should also have a phase near  $\pm\pi$  rather than near zero.

In practice, at any given frequency there will be an angular spectrum of wave vectors present and hence any averaging, whether geometric or arithmetic, will introduce some errors. However, for a single wave vector the geometric mean is exact and it has been our experience that the geometric mean provides superior results for nearly all discretizations and scattering angles. The following section demonstration the use of the geometric mean in several scenarios.

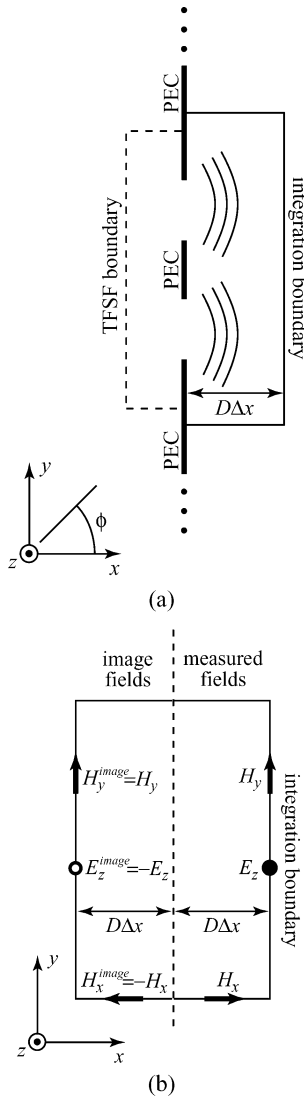


Fig. 2. (a) Geometry of the double-slit experiment. A pulsed planewave is introduced via a TFSF boundary on the left side of the screen. The fields are recorded over the three-sided integration boundary to the right of the screen. (b) Image theory is used to create a four-sided closed surface over which the currents are transformed to the far-field. The dashed line corresponds to the location where the PEC plane had been.

### III. RESULTS

#### A. Double-Slit Radiation

To demonstrate the difference between the arithmetic and geometric mean, we begin by considering the radiation from a double-slit aperture in a perfect electrical-conductor (PEC) screen which is illuminated by a normally incident pulsed planewave.  $TM^z$  polarization is assumed. As shown in Fig. 2(a), in this case the boundary over which the fields are measured is three-sided and exists on only one side of the screen.

Given the fields over the three-sided boundary, one then assumes the fields “interior” to this boundary (i.e., the region which includes the slits) are zero while the fields exterior to the boundary are unchanged. To account for the discontinuity in

the fields across the integration boundary, surface currents must be present. Since the fields are zero within the boundary, one can replace the actual interior with anything without affecting the exterior fields. One thus assumes that the slits are not present—that the PEC plane is unbroken. The surface currents over the three-sided boundary are now radiating in the presence of an infinite plane. The far-field radiation can be calculated with a three-sided integral where one uses the Green’s function for a source above an infinite plane. This, equivalently, from image theory, is simply the radiation from the original (measured) current and the image of the current. Both the measured current and the image current are radiating in free space. In this way the three-sided boundary can be replaced with a closed four-sided boundary as shown in Fig. 2(b). The corresponding currents over this surface, i.e., the measured currents over half the boundary and the image currents over the other half, are transformed to the far field. The incident field is introduced over a total-field/scattered-field (TFSF) boundary which only exists to the left side of the screen. The grid is terminated with an eight-cell perfectly matched layer (PML).

The right side of the integration surface is  $D$  cells away from the PEC screen. The length of the right side of the integration boundary is held fixed at 75 cells. In principle, the location of the integration boundary should make no difference to the far-fields. However, when using the arithmetic mean, the far-fields are sensitive to the boundary location, i.e., sensitive to the value of  $D$ . Note that were a single component of the field integrated over the aperture, as advocated by [10], averaging is not an issue. However, that approach is restricted to screens which are planar and there are no inhomogeneities present other than the screen. The approach we advocate can accommodate any screen or scatterer geometry provided it can be contained within the integration boundary. Nevertheless, we will employ the aperture-based approach as a reference solution.

The simulation uses “slits” which are 15 cells wide. The PEC between the slits is 30 cells wide. The excitation is a Ricker wavelet discretized such that there are 30 cells per wavelength at the most energetic frequency. The simulation is run at the 2-D Courant limit ( $1/\sqrt{2}$ ) for 1024 time steps.

Fig. 3(a) shows the far-field radiation pattern which is obtained using the arithmetic mean. The pattern is symmetric about zero degrees which corresponds to the direction normal to the screen. The radiation pattern is calculated using

$$\frac{1}{\lambda} \lim_{\rho \rightarrow \infty} \left[ 2\pi\rho \frac{|\hat{E}_z(\phi)|^2}{|\hat{E}_z^i|^2} \right] \quad (26)$$

where  $\phi$  is the scattering angle,  $\rho$  is the distance from the slits,  $\hat{E}_z(\phi)$  is the field radiated in the  $\phi$  direction, and  $\hat{E}_z^i$  is the complex amplitude of the incident planewave at the frequency of interest. Results are shown for a frequency corresponding to 10.0566 cells per wavelength. Fig. 3(a) shows the pattern when  $D$  is either 5, 6, or 7 cells.

Note that there are significant differences in the central peak depending on the displacement  $D$  between the right-side integration boundary and the PEC screen. Fig. 3(b) shows an expanded view of the pattern in the neighborhood of the peak. As can be seen, displacing the integration boundary by two cells

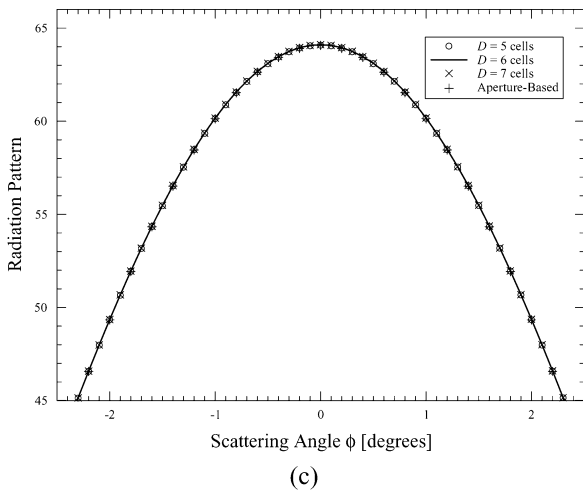
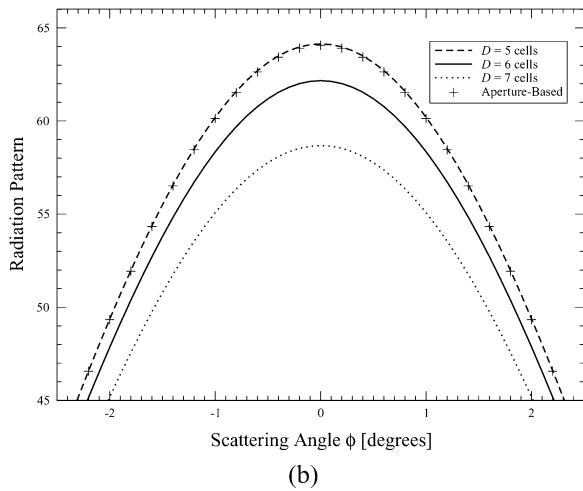
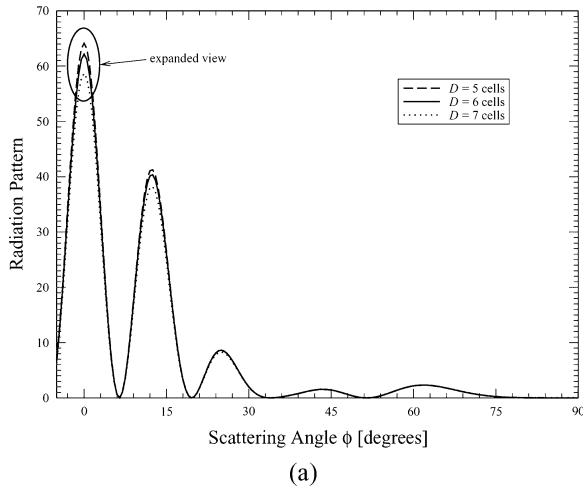


Fig. 3. (a) Radiation from the double slit for angles between  $-5$  and  $90$  deg. (the pattern is symmetric about  $0$  deg.). Results are shown for boundary displacements  $D$  of 5, 6, and 7 cells. The arithmetic mean is used. (b) Expanded view of the central peak using the arithmetic mean. Also shown are the fields obtained when a single field component is recorded over the aperture and transformed to the far field. (c) Same as (b) except the geometric mean is used. The variation of the fields caused by the displacement of the boundary is now essentially negligible.

causes a change in the peak of approximately 9 percent. The results as a function of displacement are nearly periodic, e.g., displacements of 5 and 15 cells (not shown) yield nearly the same

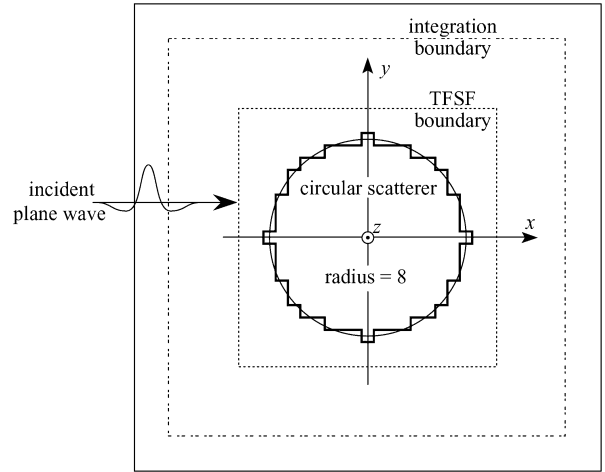


Fig. 4. Geometry of the circular PEC cylinder.

results as do displacements of 6 and 16 cells, and so on. (The period of 10 cells is a consequence of examining a frequency corresponding to approximately 10 cells per wavelength.) Also shown as plus signs in Fig. 3(b) are the results obtained when the transform uses the electric field (i.e., the equivalent magnetic current) over the aperture. No averaging is involved in this case. The aperture-based results are seen to agree well with the arithmetic-mean results when the displacement  $D$  is 5 cells. Unfortunately one does not know *a priori* that this agreement will exist nor does this displacement provide similar agreement for other frequencies.

On the other hand, when using the geometric mean, there is almost no variation in the radiation pattern as the integration boundary is displaced. Fig. 3(c) shows the same results as presented in Fig. 3(b) except now the geometric mean of the harmonic fields is used to obtain the magnetic fields on the integration boundary. The variation between these peaks is less than 0.022, i.e., a reduction in variation by a factor of approximately 270. This demonstrates that, unlike with the arithmetic mean, the location of the integration boundary is effectively irrelevant when using the GM-NTFF transform.

Naturally, at finer discretizations, the difference between the geometric mean and the arithmetic mean are less dramatic, but the geometric mean consistently performs better than the arithmetic mean. (Simpson's rule was used for all integrations except for the integration of the aperture fields where a Riemann sum was used.)

### B. Scattering From a Circular Cylinder

Consider scattering from a PEC circular cylinder under  $TM^z$  polarization as shown in Fig. 4. The Dey-Mittra scheme is employed to help reduce the effects of staircasing [24]. The cylinder has eight cells along its radius. A pulsed planewave which travels in the  $x$  direction is introduced via a TFSF boundary. The simulation is run 512 time steps. Because the Dey-Mittra scheme is used, the Courant number was reduced to approximately 35% of the 2-D limit in order to ensure stability [25].

Fig. 5 shows the wavelength-normalized scattering width of the cylinder as a function of scattering angle obtained using the

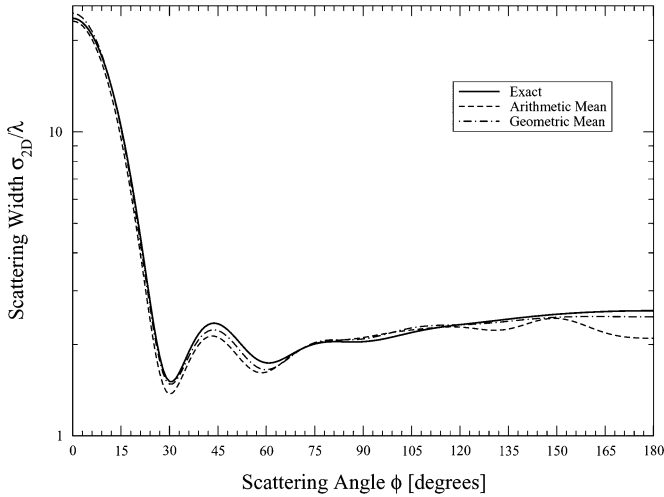


Fig. 5. Scattering width of a circular cylinder. The radius is 8 cells and the frequency corresponds to 9.92526 cells per wavelength.

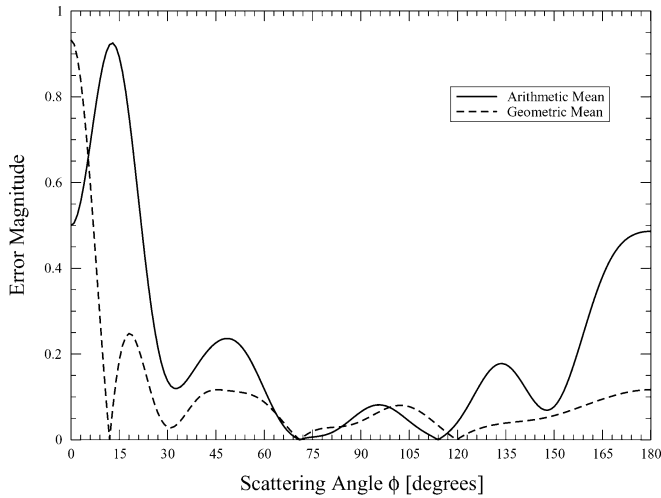


Fig. 6. Magnitude of the difference between the FDTD-based solutions and the nominally exact solution.

series solution for a circular cylinder [2], the arithmetic-mean NTFF transform, and the GM-NTFF transform. (The normalized scattering width is the same as the radiation pattern given in (26) where  $\rho$  is now taken to be the distance from the center of the cylinder.) The discretization is such that there are 9.92526 cells per wavelength at the frequency being considered here. One should keep in mind that the discretization of the cylinder introduces some errors and hence the “exact” solution for a circular cylinder is not truly exact for the scatterer present in the simulation. Therefore, the reference solution does not provide a perfect way with which to judge the solutions. Nevertheless, one hopes that the FDTD scatterer, when employing the Dey–Mittra scheme, is a close approximation to a true circular scatterer and thus the exact solution from the continuous world provides a reasonable basis for comparison.

The difference between the solutions in Fig. 5 are seen to be relatively small. Fig. 6 shows a plot of the magnitude of the difference between the exact solution and the FDTD-based solutions. Although there are angles where the arithmetic mean performs better than the geometric mean, in general the geometric

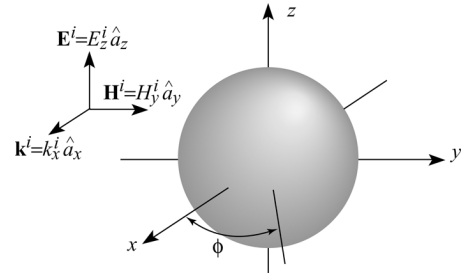


Fig. 7. Geometry of the dielectric sphere. The relative permittivity  $\epsilon_r$  is 1.21. This incident field is polarized in the  $z$  direction and travels in the  $x$  direction. The equatorial angle  $\phi$  is in the  $xy$ -plane with  $\phi = 0$  corresponding to the  $+x$  direction.

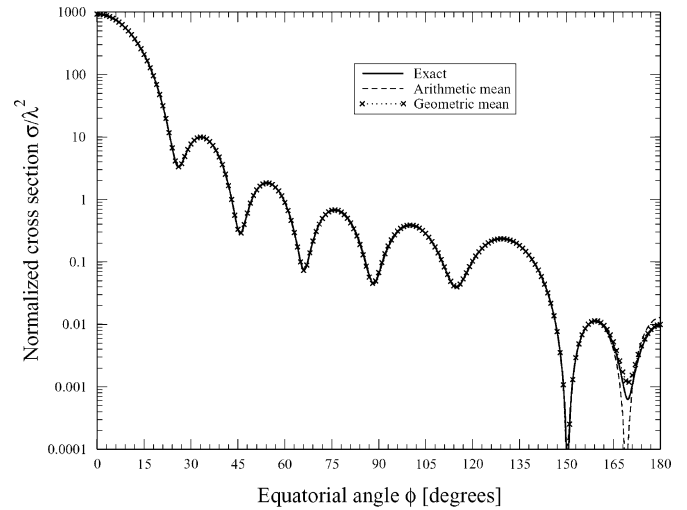


Fig. 8. Scattering cross section of a dielectric sphere versus the equatorial angle  $\phi$ . The sphere is discretized with 60 cells along the radius and the frequency used here corresponds to 20.06 cells per wavelength.

mean is better. The integrated error for angles between 0 and  $\pi$  is 0.6936 for the arithmetic mean and 0.3221, i.e., the error is reduced by more than a factor of two by using the geometric mean.

### C. Scattering From a Strongly Forward-Scattering Sphere

Finally, consider scattering from a dielectric sphere, depicted in Fig. 7, which has a relative permittivity  $\epsilon_r$  of 1.21. Such a sphere was considered in [20] and can also be found in [19, Section 8.7]. In this case the transformation traditionally entails finding the tangential fields over the six sides of a cuboid which bounds the sphere. The sphere is discretized such there are 60 cells along the radius. A staircase representation is used (where a node is simply either inside or outside the sphere). The simulation is run at 95% of the 3-D Courant limit ( $0.95/\sqrt{3}$ ) for 2048 time steps. The grid is terminated with an eight-cell PML.

Fig. 8 shows the normalized scattering cross section as a function of the equatorial angle  $\phi$ . The frequency corresponds to 20.06 cells per wavelength. The exact solution was obtained via the Mie series (see, e.g., [26]). As was the case in 2-D, both the arithmetic and geometric mean perform reasonably well, but the geometric mean is generally more accurate than the arithmetic mean. In Fig. 8, visible errors are only present near the back-scattering direction of  $\phi = 180$  degrees. Note that there is

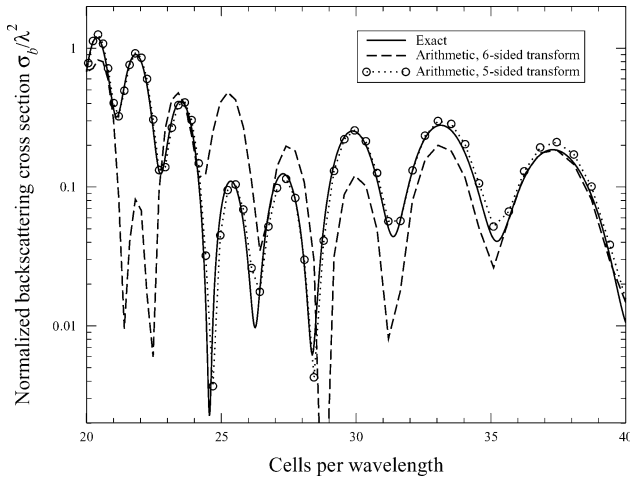


Fig. 9. Backscatter from a sphere with  $\epsilon_r = 1.21$  versus the wavelength (expressed in terms of number of cells). The FDTD transformations are calculated using the arithmetic mean and either a five- or six-sided transformation boundary.

a large difference, approximately five orders of magnitude, between the scattering in the forward and backward directions.

In order to improve the results in the back-scattering direction Li *et al.* [20] advocated calculating the transformation using the five faces other than the forward-scattering face. Fig. 9 shows the normalized backscattering cross section versus wavelength (expressed in terms of number of cells per wavelength) calculated using the arithmetic mean. The normalized cross section is given by

$$\frac{1}{\lambda^2} \lim_{r \rightarrow \infty} \left[ 4\pi r^2 \frac{|\hat{E}_z(\theta, \phi)|^2}{|\hat{E}_z^i|^2} \right] \quad (27)$$

where  $r$  is the distance from the center of the sphere,  $\theta$  is the azimuthal angle and  $\phi$  is the equatorial angle. For backscatter,  $\theta$  is  $\pi/2$  and  $\phi$  is  $\pi$ .

The NTFF transform results shown in Fig. 9 were calculated using either the fields over all six faces of the integration boundary or the fields over the five faces advocated by Li *et al.* The results in this figure correspond to those shown in Fig. 1(b) of [20] for the sphere with a radius of  $3 \mu\text{m}$ . (However, for the sake of generality, here the results are plotted in terms of unitless quantities.) Note that the six-sided arithmetic-mean results presented here are better than those presented in [20]. We were able to duplicate the results presented in [20] by not applying a temporal phase-correction factor (or, similarly, by applying a correction factor which is twice the factor given here). Nevertheless, the recommendation of Li *et al.* is true that the five-sided computation is better than the six-sided one for calculating the backscattering when using the arithmetic mean. However, for directions other than backscatter or for other sizes, one does not know *a priori* if a face should or should not be discarded.

Fig. 10 is the same as Fig. 9 except the transformation is done using the GM-NTFF transform. In this case discarding data from the forward-scattering face actually slightly degrades the quality of the transform. Thus, when using the geometric mean there is no need to discard data. One can use it confidently for all scattering angles and all sizes.

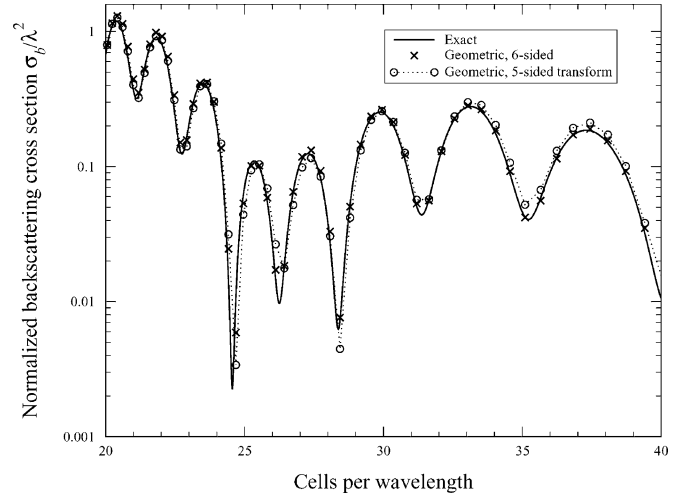


Fig. 10. Backscatter from a sphere with  $\epsilon_r = 1.21$  versus the wavelength (expressed in terms of number of cells). The transformations use the geometric mean and the fields over either five or six faces of the integration boundary.

#### IV. CONCLUSION

Unlike the traditional arithmetic mean, for a single harmonic planewave the geometric mean accounts for the spatial offset of the fields in a way that is exact. In practice, where a spectrum of wave vectors are present, the geometric mean typically performs significantly better than the arithmetic mean. The geometric mean is much less sensitive to the integration-boundary location than is the arithmetic mean. For strongly forward-scattering objects, the use of the geometric mean obviates the need to discard the fields over the forward face (as has been advocated previously) when calculating backscatter. The geometric mean does entail a slight increase in computational cost because for each node along the integration boundary a DFT must be calculated for three fields instead of two. However, this cost is typically minor compared to the overall simulation cost.

#### REFERENCES

- [1] S. A. Schelkunoff, "Some equivalence theorems of electromagnetics and their application to radiation problems," *Bell Syst. Techn. J.*, vol. 15, pp. 92–112, 1936.
- [2] C. A. Balanis, *Advanced Engineering Electromagnetics*. New York: Wiley, 1989.
- [3] K. R. Umashankar and A. Taflove, "A novel method to analyze electromagnetic scattering of complex objects," *IEEE Trans. Electromagn. Compat.*, vol. EMC-24, no. 4, pp. 397–405, Nov. 1982.
- [4] A. Taflove and K. Umashankar, "Radar cross section of general 3-D scatterers," *IEEE Trans. Electromagn. Compat.*, vol. EMC-25, no. 4, pp. 662–666, Nov. 1983.
- [5] A. Taflove, K. R. Umashankar, and T. G. Jurgens, "Validation of FD-TD modeling of the radar cross section of 3-D structures spanning up to nine wavelengths," *IEEE Trans. Antennas Propag.*, vol. 33, no. 6, pp. 662–666, Jun. 1985.
- [6] S. M. Lee, W. C. Chew, M. Moghaddam, M. A. Nasir, S.-L. Chuang, R. W. Herrick, and C. L. Balestra, "Modeling of rough-surface effects in an optical turning mirror using the finite-difference time-domain method," *J. Lightw. Technol.*, vol. 9, no. 11, pp. 1471–1480, Nov. 1991.
- [7] C. M. Furse, S. P. Mathur, and O. P. Gandhi, "Improvements to the finite-difference time-domain method for calculating the radar cross section of a perfectly conducting target," *IEEE Trans. Microw. Theory Techn.*, vol. 38, no. 7, pp. 919–927, Jul. 1990.
- [8] K. Demarest, Z. Huang, and R. Plumb, "An FDTD near- to far-zone transformation for scatterers buried in stratified grounds," *IEEE Trans. Antennas Propag.*, vol. 44, no. 8, pp. 1150–1157, Aug. 1996.

- [9] Z. Huang, K. R. Demarest, and R. G. Plumb, "An FDTD/MoM hybrid technique for modeling complex antennas in the presence of heterogeneous grounds," *IEEE Trans. Geosci. Remote Sens.*, vol. 37, no. 6, pp. 2692–2698, Nov. 1999.
- [10] D. Sullivan and J. L. Young, "Far-field time-domain calculation from aperture radiators using the FDTD method," *IEEE Trans. Antennas Propag.*, vol. 49, no. 3, pp. 464–469, Mar. 2001.
- [11] K. S. Kunz, "An improved near to far field FDTD algorithm," in *Proc. 11th Annu. Rev. Progress in Applied Computational Electromagnetics*, Monterey, CA, Mar. 1995, vol. 1, pp. 431–434.
- [12] C. L. Britt, "Solution of electromagnetic scattering problems using time domain techniques," *IEEE Trans. Antennas Propag.*, vol. 37, no. 9, pp. 1181–1192, Sep. 1989.
- [13] K. S. Yee, D. Ingham, and K. Shlager, "Time-domain extrapolation to the far field based on FDTD calculations," *IEEE Trans. Antennas Propag.*, vol. 39, no. 3, pp. 410–413, Mar. 1991.
- [14] R. J. Luebbers, K. S. Kunz, M. Schneider, and F. Hunsberger, "A finite-difference time-domain near zone to far zone transformation," *IEEE Trans. Antennas Propag.*, vol. 39, no. 4, pp. 429–433, Apr. 1991.
- [15] M. J. Barth, R. R. McLeod, and R. W. Ziolkowski, "A near and far-field projection algorithm for finite-difference time-domain codes," *J. Electromagn. Waves Appl.*, vol. 6, no. 1, pp. 5–18, 1992.
- [16] K. L. Shlager and G. S. Smith, "Near-field to near-field transformation for use with FDTD method and its application to pulsed antenna problems," *Electron. Lett.*, vol. 30, no. 16, pp. 1262–1264, Aug. 1994.
- [17] K. L. Shlager and G. S. Smith, "Comparison of two FDTD near-field to near-field transformations applied to pulsed antenna problems," *Electron. Lett.*, vol. 31, no. 12, pp. 936–938, Jun. 1995.
- [18] M. Kragalott, M. S. Kluskens, and W. P. Pala, "Time-domain fields exterior to a 2-D FDTD space," *IEEE Trans. Antennas Propag.*, vol. 45, no. 11, pp. 1655–1663, Nov. 1997.
- [19] A. Taflove and S. Hagness, *Computational Electrodynamics: The Finite-Difference Time-Domain Method*, 3rd ed. Norwood, MA: Artech House, 2005.
- [20] X. Li, A. Taflove, and V. Backman, "Modified FDTD near-to-far-field transformation for improved backscattering calculation of strongly forward-scattering objects," *IEEE Antennas Wireless Propag. Lett.*, vol. 4, pp. 35–38, 2005.
- [21] J. Fang and D. Xeu, "Numerical errors in the computation of impedances by FDTD method and ways to eliminate them," *IEEE Microw. Guided Wave Lett.*, vol. 5, no. 1, pp. 6–8, Jan. 1995.
- [22] N. Dib, M. Krumpholz, E. Tentzeris, and L. P. B. Katehi, "Comments on 'Numerical errors in the computation of impedances by FDTD method and ways to eliminate them'," *IEEE Microw. Guided Wave Lett.*, vol. 5, no. 10, p. 354, Oct. 1995.
- [23] J. Fang and D. Xue, "Reply to comments on 'Numerical errors in the computation of impedances by FDTD method and ways to eliminate them'," *IEEE Microw. Guided Wave Lett.*, vol. 5, no. 10, pp. 354–355, Oct. 1995.
- [24] S. Dey and R. Mittra, "A locally conformal finite-difference time-domain (FDTD) algorithm for modeling 3-D perfectly conducting objects," *IEEE Microw. Guided Wave Lett.*, vol. 7, no. 9, pp. 273–275, Sep. 1997.
- [25] S. Benkler, N. Chavannes, and N. Kuster, "A new 3-D conformal PEC FDTD scheme with user-defined geometric precision and derived stability criterion," *IEEE Trans. Antennas Propag.*, vol. 54, no. 6, pp. 1843–1849, Jun. 2006.
- [26] A. Ishimaru, *Electromagnetic Wave Propagation, Radiation, and Scattering*. Englewood Cliffs, NJ: Prentice Hall, 1991.

**Dirk J. Robinson** received the M.S. degree in physics in 2005 at Washington State University, Pullman, where he is currently pursuing the Ph.D. degree in electrical engineering. His research is in high-speed analog to digital conversion using SiGe technology.

**John B. Schneider** (M'91) received the B.S. degree in electrical engineering from Tulane University, New Orleans, LA, and the M.S. and Ph.D. degrees in electrical engineering from the University of Washington, Seattle.

He is presently an Associate Professor in the School of Electrical Engineering and Computer Science at Washington State University, Pullman. His research interests include the use of computational methods to analyze acoustic, elastic, and electromagnetic wave propagation.